

Mott insulator state in a van der Waals flat-band compound

Shunye Gao,^{1,2,3,#} Shuai Zhang,^{1,2,#} Cuixiang Wang,^{1,2,#} Wei Tao,¹ Jingtong Liu,¹ Tiantian Wang,¹ Shuaikang Yuan,¹ Gexing Qu,^{1,2} Mojun Pan,^{1,2} Shiyu Peng,^{1,2} Yong Hu,³ Hang Li,³ Yaobo Huang,⁴ Hui Zhou,^{1,2} Sheng Meng,^{1,2,5} Liu Yang,^{6,7} Zhiwei Wang,^{6,7,8} Yugui Yao,^{6,7} Zhiguo Chen,^{1,5} Ming Shi,³ Hong Ding,^{1,2,5} Kun Jiang,^{1,2,5} Yunliang Li,^{1,2,5} Youguo Shi,^{1,2,5,*} Hongming Weng,^{1,2,5,*} Tian Qian,^{1,5,*}

¹ *Beijing National Laboratory for Condensed Matter Physics and Institute of Physics, Chinese Academy of Sciences, Beijing, 100190, China*

² *University of Chinese Academy of Sciences, Beijing, 100049, China*

³ *Photon Science Division, Paul Scherrer Institut, CH-5232 Villigen, Switzerland*

⁴ *Shanghai Synchrotron Radiation Facility, Shanghai Advanced Research Institute, Chinese Academy of Sciences, Shanghai, 201204, China*

⁵ *Songshan Lake Materials Laboratory, Dongguan, Guangdong, 523808, China*

⁶ *Centre of Quantum Physics, Key Laboratory of Advanced Optoelectronic Quantum Architecture and Measurement, Ministry of Education, School of Physics, Beijing Institute of Technology, Beijing 100081, China*

⁷ *Micronano Center, Beijing Key Lab of Nanophotonics and Ultrafine Optoelectronic Systems, Beijing Institute of Technology, Beijing 100081, China*

⁸ *Material Science Center, Yangtze Delta Region Academy of Beijing Institute of Technology, Jiaxing, 314011, China*

[#] These authors contributed equally to this work.

^{*} Corresponding authors: tqian@iphy.ac.cn, hmweng@iphy.ac.cn, ygshi@iphy.ac.cn

Abstract

When many-body effects dominate over the kinetic energy of electrons, they will lead to exotic quantum phenomena, such as the fractional quantum Hall effect, unconventional superconductivity, Mott insulator, quantum spin liquid, ferromagnetism, heavy fermion behavior and so on. Flat-band systems, in which the kinetic energy is strongly quenched, are promising for realizing many-body quantum phases, such as the Mott-like insulator states and unconventional superconductivity associated with the flat bands emerging in twisted bilayer graphene. In this work, we have discovered a room-temperature Mott insulator state, which is derived from a half-filled flat band in a van der Waals compound Nb_3Cl_8 . Since the half-filled flat band is well separated from the other bands, the Mott insulator state in Nb_3Cl_8 is a straightforward realization of the celebrated single-band Hubbard model. Our discovery provides an intriguing platform for studying the fundamental physics of Mott insulator, and paves the way for more correlated electronic states and Mott insulator-based devices by taking advantage of the high tunability of the electronic states of two-dimensional materials.

I. INTRODUCTION

Strongly correlated electron systems have always been the focus in the field of condensed matter physics in recent decades because of their exotic and rich physical phenomena as well as tremendous potential for practical applications. In strongly correlated systems, the electron-electron interactions exceed the kinetic energy of electrons. Since the kinetic energy is associated with the one-electron bandwidth, flat-band systems are a promising platform for realizing various correlated electronic states [Fig. 1(a)] [1–15].

Heavy-fermion compounds are a class of typical strongly correlated systems with flat bands [15]. The flat bands are formed by localized f orbitals, where the kinetic energy of electrons is extremely suppressed by small overlap between atomic wave functions. In certain geometrically frustrated structures, such as kagome [16–19] and Lieb lattices [20], the kinetic energy is quenched due to the destructive interference of electron wave functions, resulting in non-dispersive flat bands. Angle-resolved photoemission spectroscopy (ARPES) experiments have shown flat bands in materials with the two-dimensional (2D) kagome lattice [21–25], while correlation-induced physical phenomena associated with these flat bands still remain to be explored.

Recently, flat bands have been realized in a van der Walls (vdW) heterostructure, *i.e.*, magic-angle twisted bilayer graphene [26,27]. The electron wave functions are localized in the moiré pattern produced by the lattice misorientation at a certain twist angle. The quenching of the kinetic energy results in flat bands near the Fermi level (E_F). By tuning the flat bands in a variety of ways, exotic correlated states such as Mott-like insulator states and unconventional superconductivity have been revealed [26–30].

The flat bands of twisted bilayer graphene are generated by the interlayer hybridization between misoriented monolayers, while graphene itself is a well-known 2D Dirac material with linear band dispersion [31]. Here, we have revealed that in the vdW compound Nb_3Cl_8 charge localization results in intrinsic flat bands within each monolayer. As the flat band at E_F is half filled, the Coulomb repulsion greatly exceeds

the kinetic energy, driving the system into a Mott insulator state. The Mott insulator state is derived from a single half-filled band, making it a paradigm system that is described by the single-band Hubbard model.

II. RESULTS

Nb_3Cl_8 is a layered compound with space group $P\bar{3}m1$ (No. 164) at room temperature [32,33]. Each unit cell contains two Nb_3Cl_8 monolayers stacked along c axis via weak vdW force [Fig. 1(b)]. The Nb ions in each monolayer form the breathing kagome lattice, in which three Nb ions are close to each other to form a Nb_3 trimer [Fig. 1(c)] [33,34]. Each Nb_3 trimer is surrounded by a total of thirteen Cl ions to form a $\text{Nb}_3\text{Cl}_{13}$ cluster composed of three edge-sharing NbCl_6 octahedra [Fig. 1(d)]. The intracluster Nb–Nb distance $d_1 = 2.834$ Å is substantially shorter than the intercluster Nb–Nb distance $d_2 = 3.998$ Å [33], indicating the formation of Nb–Nb metal bonds within each cluster. The octahedral crystal field splits the Nb 4d orbitals into e_g and t_{2g} orbitals, which form molecular orbitals in an isolated $\text{Nb}_3\text{Cl}_{13}$ cluster as a result of the metal bonds [Fig. 1(e)]. The strong electronegativity of the Cl ions results in a valence state of $[\text{Nb}_3]^{8+}$ with seven valence electrons. Six valence electrons fill the lowest three molecular orbitals, while the seventh electron occupies the $2a_1$ orbital and remains unpaired [33,35].

Figure 1(f) shows the first-principles band structure for monolayer Nb_3Cl_8 calculated with the Heyd-Scuseria-Ernzerhof (HSE06) functional, which is improved as compared with those from local density approximation or generalized gradient approximation. It can be seen that the molecular orbitals form flat bands with weak dispersion. The bandwidth is determined by the overlap between Nb 4d orbitals and 3p orbitals of the ligand Cl ions that bridge adjacent Nb_3 clusters. The indirect transfer between d orbitals through ligand p orbitals strongly suppresses the kinetic energy of electrons. Because of the odd number of valence electrons, E_F lies within a half-filled flat band formed by the $2a_1$ molecular orbital. We note that although there are two

monolayers in one unit cell for bulk Nb_3Cl_8 , the double layer has negligible effects on the electronic structure due to the extremely weak interlayer hybridization. For simplicity, our analysis is based on the electronic states of the monolayer, which capture the main features of the bulk.

The above band structure obtained within single-particle approximation indicates that Nb_3Cl_8 has a metallic electronic state with a half-filled band at E_F [Fig. 2(a)], whereas our ARPES results show an obvious gap [Figs. 2(b) and 2(c)], which is consistent with the insulating behavior in previous transport measurements [36]. We found that even though the ARPES experiments were carried out at room temperature, the spectra suffer from charging effects, that is, the kinetic energy of photoelectrons decreases with the increase of photon flux. Therefore, the gap between the topmost valence band and E_F , which was calibrated by measuring the clean gold samples, is overestimated.

Except for the half-filled band at E_F , the experimental bands are in good agreement with the calculations over a wide energy range. The calculations show that the valence band structure consists of two sets of well separated bands. One set from the Cl $3p$ orbitals lies far below E_F due to strong electronegativity of the Cl ions, while another at lower binding energies is from the Nd $4d$ orbitals. The photon energy ($h\nu$)-dependent data in Fig. 2(d) exhibit that the spectral intensities of the bands within 3 eV below E_F are significantly suppressed around $h\nu = 32$ eV, which is attributed to the Nb $4p$ - $4d$ antiresonance, confirming that the bands are contributed by the Nb $4d$ orbitals.

To determine the gap size at E_F , we have measured photoluminescence spectroscopy (PL) using a pulsed laser. The PL spectrum excited by 1.1-eV photons exhibits two peaks around 0.7 and 1.0 eV, respectively [Fig. 2(e)]. The splitting of the peaks is due to the slit between pixels on the detector. In contrast, the 0.7-eV peak vanishes in the PL spectrum excited by 0.75-eV photons in Fig. 2(f), suggesting that the state at 0.7 eV above the valence band is not an intrinsic band. The 1.0-eV peak is attributed to the recombination of photoexcited electrons on the conduction bands and holes on the valence bands, indicating that the gap size at E_F is about 1.0 eV in Nb_3Cl_8 .

To understand the origin of the insulating electronic state, we compare the experimental and calculated band dispersions in detail in Fig. 3. We find that the spectral intensities are sensitive to the polarization of the incident light due to the matrix element effects. Combining the ARPES data collected with horizontally and vertically polarized light, we identify a total of four bands within 3 eV below E_F in agreement with the calculations [Figs. 3(a)–3(d)]. For convenience, the four bands are denoted as b1, b2, b3, and b4. The ARPES spectra are shifted up by 0.2 eV to better match the calculations. The energy shift is acceptable since the charging effects reduce the kinetic energy of photoelectrons.

We extract the experimental band dispersions for precise comparison with the calculations in Fig. 3(e). The filled b2, b3 and b4 band dispersions are almost identical between experiment and calculation. In contrast, the calculated b1 band has to be shifted down by 0.72 eV to match the experimental one, and even so we find that they do not agree well. The calculated b1 band is renormalized by a factor of 1.6 to obtain the best match [Fig. 3(f)]. The band renormalization indicates that strong correlation effects on the half-filled b1 band must be considered beyond the above single-particle approximation. The on-site Coulomb repulsion (U) on the $4d$ orbitals is on the order of 1 eV [37], which is significantly larger than the one-electron bandwidth of 0.28 eV for the b1 band. A Mott transition could happen on the half-filled flat band, resulting in the insulating electronic state, where the observed b1 band below E_F is attributed to the lower Hubbard band.

To describe the Mott-Hubbard physics in Nb_3Cl_8 , we have performed dynamical mean-field theory (DMFT) calculations on the b1 band. Since there is only one single half-filled band near E_F , the single-band Hubbard model can be applied. We calculate the imaginary time Green's function with $U = 1$ eV in Fig. 4(a). On the basis of this result, we obtain the density of states (DOS) [Fig. 4(b)] and band dispersions along high-symmetry path [Fig. 4(c)] of the single-band Hubbard model. Despite the moderate value of U , the system is driven into a Mott insulator state because the kinetic energy is quenched on the flat b1 band. The half-filled b1 band is split into the so-called

upper and lower Hubbard bands with the gap size dictated by the value of U . In the Mott insulator state, the one-electron band is renormalized by a factor of 1.7, which is consistent with our ARPES results.

III. SUMMARY

The significant gap opening on the half-filled flat band with an appreciable band renormalization establishes Nb_3Cl_8 as a canonical Mott insulator. The Mott insulator state involves only one single band isolated from the high-energy bands, thus providing an excellent platform for studying the typical physics of the single-band Hubbard model. As one unpaired electron is localized in each Nb_3 cluster due to the long distance between clusters, the quenching of the kinetic energy leads to the Mott transition. Such a Mott transition is a straightforward manifestation of the Mott physics in his thought experiment [8]. The Mott insulator state exists naturally at room temperature, and its generation does not require sophisticated manipulation. Because of the weak vdW coupling, Nb_3Cl_8 crystals can be easily exfoliated into few-layer or even monolayer flakes [36]. It is convenient to study and control the Mott insulator state through a variety of physical and chemical methods. For instance, the Mott insulator state can be tuned by external electric field or strain at the 2D limit, facilitating filling- or bandwidth-control transitions to other correlated states. Lastly, we mention that the magnetic-field-free Josephson diode has recently been realized in a van der Waals heterostructure based on its sister material Nb_3Br_8 [38,39]. It is feasible and desirable to fabricate Mott insulator-based devices with this family of materials to produce more exotic quantum phenomena.

Method

High quality single crystals of Nb_3Cl_8 were growth using PbCl_2 as the flux. The starting materials of Nb (Alfa Aesar, 99.99 %), NbCl_5 (Alfa Aesar, 99.9 %) were mixed with a molar ratio of 7:8 in a glovebox filled by argon. The mixture was placed in an alumina crucible and sealed in quartz tube under vacuum. The whole device was heated to 750 °C for 150 hours, and then was cooled to room temperature. Finally, the single crystals were separated from the PbCl_2 flux with hot water.

ARPES experiments were performed at the “Dreamline” beamline of Shanghai Synchrotron Radiation Facility, the APE-LE beamline of the Elettra Light Source (proposal 20215821), the SIS-ULTRA beamline of the Swiss Light Source, the 13U ARPES beamline of the National Synchrotron Radiation Laboratory at Hefei (proposal 2021-HLS-PT-004344), the “Bloch” beamline of MAXIV at Sweden (proposal 20200353), and the “UARPES” beamline of SOLARIS at Poland (proposal 211070). The samples were cleaved *in situ* and measured at $h\nu = 40$ eV except for the $h\nu$ dependence measurements. E_F was calibrated by measuring the clean gold samples. To alleviate the charging effects, the experiments were carried out at room temperature with low photon flux.

1 KHz pulse train of 90 fs centered at 800 nm with 3 mJ output are generated by a Ti:sapphire regenerative amplifier (Spectra-Physic, Spitfire) seeded with an oscillator (Spectra-Physics, spitfire). Approximately 70% of the output is used to pump the commercially automated optical parametric amplifier (TOPAS, Spectra-Physic, Spitfire), which can produce the infrared (IR) light tunable from 1.1 to 2.6 um with 200 uJ pulse energy, and the wavelength ranging from 800 nm to 1 um was further generated by transmitting the IR pulse into a beta-barium borate crystal (BBO). The visible light varying from 266 to 760 nm was produced with a home-build non-collinear optical parametric amplifier (NOPA) system. The light with selected wavelength and optimized energy was focused onto the sample with a 150-um spot size, and the scattered signal from the sample surface was collected by a 64-channel Mid-IR detector (FPAS

0144 Infrared systems development) combining with 300 mm focal length spectrometer (Princeton instrument 2300i). For revealing the band gap, the sample was symmetrically irradiated with different central wavelength varying from 400 nm to 1.5 um.

We employed the Vienna *Ab initio* Simulation Package (VASP) [40] to perform the electronic structure calculations. The projector-augmented-wave (PAW) [41,42] method with HSE06 functional [43,44] was used. The plane-wave cutoff for kinetic energy was set as 500 eV, and a $6 \times 6 \times 1$ Γ -centered Monkhorst-Pack k -point mesh was used to sample the Brillouin zone in the self-consistent charge convergence calculation. For calculating the DOS more efficiently, we constructed the Wannier functions for the bands composed of the Nb 4d and Cl 3p orbitals using the Wannier90 package [45]. The crystal structure used in the calculations is from Ref. [33].

We performed DMFT calculations [46] on the single-band Hubbard model using the IQIST package [47], which employs the continuous-time quantum Monte Carlo (CTQMC) [48] impurity solver to solve the impurity imaginary time Green's function. Because of the absence of magnetic order in this material, we will focus on the nonmagnetic phase in the DMFT calculations and ignored the spin-orbital coupling (SOC) effect for simplicity. We use the DOS obtained from the single band crossing E_F to initialize the local Green's function. The DMFT calculations were performed at temperature controlled by the parameter β of 400 corresponding to about 29.01 K. The spectral function was obtained from the analytic continuation using the maximal entropy method and Pade approximation [47,49].

Acknowledgments

We thank X.-Z. Chen, B. Jiang, J.-R. Huang, F.-M. Chen, J.-D. Liu, I. Vobornik, J. Fuji, N. C. Plumb, A. Pfister, H.-E. Zhu, C. Polley and N. Olszowska for technical assistance. This work was supported by the Ministry of Science and Technology of China (2018YFA0305700, 2020YFA0308800, 2017YFA0403401), the National Natural

Science Foundation of China (U1832202, 11925408, 11921004, 12188101, 22073111, 11734003, 11888101, 12025407, 12061131002, U2032204, 92065109), the Chinese Academy of Sciences (QYZDB-SSW-SLH043, XDB33000000, XDB28000000), the Informatization Plan of Chinese Academy of Sciences (CAS-WX2021SF-0102), the K. C. Wong Education Foundation (GJTD-2018-01), the Beijing Natural Science Foundation (Z180008, Z210006), the China Scholarship Council (202104910090), the Young Researchers' Exchange Programme between China and Switzerland (CN-EG-03-012021), and the Swiss National Science Foundation (200021-188413).

Reference

- [1] D. C. Tsui, H. L. Stormer, & A. C. Gossard, Two-dimensional magnetotransport in the extreme quantum limit. *Phys. Rev. Lett.* **48**, 1559-1562 (1982).
- [2] H. L. Stormer, Nobel Lecture: The fractional quantum Hall effect. *Rev. Mod. Phys.* **71**, 875-889 (1999).
- [3] C. Pfleiderer, Superconducting phases of *f*-electron compounds. *Rev. Mod. Phys.* **81**, 1551-1624 (2009).
- [4] B. Keimer, S. A. Kivelson, M. R. Norman, S. Uchida, & J. Zaanen, From quantum matter to high-temperature superconductivity in copper oxides. *Nature* **518**, 179-186 (2015).
- [5] G. R. Stewart, Superconductivity in iron compounds. *Rev. Mod. Phys.* **83**, 1589-1652 (2011).
- [6] P. A. Lee, N. Nagaosa, & X.-G. Wen, Doping a Mott insulator: physics of high-temperature superconductivity. *Rev. Mod. Phys.* **78**, 17-85 (2006).
- [7] J. Hubbard, Electron Correlations in Narrow Energy Bands. *Proc. R. Soc. A* **276**, 238 (1963).
- [8] N. F. Mott, Metal-Insulator Transitions. *Rev. Mod. Phys.* **40**, 677-783 (1968).
- [9] S. B. Roy, Mott insulators: physics and applications. *Bristol, UK: IOP publishing* (2019).
- [10] L. Balents, Spin liquid in frustrated magnets. *Nature* **464**, 199-208 (2010).
- [11] Y. Zhou, K. Kanoda, & T.-K. Ng, Quantum spin liquid states. *Rev. Mod. Phys.* **89**, 025003 (2017).
- [12] A. Mielke, Ferromagnetic ground states for the Hubbard model on line graphs. *J. Phys. A* **24**, L73-L77 (1991).

- [13] A. Mielke, & H. Tasaki, Ferromagnetism in the Hubbard model. *Commun. Math. Phys.* **158**, 341-371 (1993).
- [14] H. Tasaki, Ferromagnetism in Hubbard models with degenerate single-electron ground states. *Phys. Rev. Lett.* **69**, 1608 (1992).
- [15] Q. Si, & F. Steglich, Heavy fermions and quantum phase transitions. *Science* **329**, 1161-1166 (2010).
- [16] A. Mielke, Exact ground states for the Hubbard model on the kagome lattice. *J. Phys. A* **25**, 4335-4345 (1992).
- [17] D. Calugaru *et al.*, General Construction and topological classification of crystalline flat bands. *Nat. Phys.* **18**, 185-189 (2022).
- [18] N. Regnault *et al.*, Catalogue of flat-band stoichiometric materials. *Nature* **603**, 824-828 (2022).
- [19] H. Liu, S. Meng, and F. Liu, Screening two-dimensional materials with topological flat bands. *Phys. Rev. Mater.* **5**, 084203 (2021).
- [20] E. H. Lieb, Two theorems on the Hubbard model. *Phys. Rev. Lett.* **62**, 1201-1204 (1989).
- [21] Z. Lin *et al.*, Flatbands and emergent ferromagnetic ordering in Fe_3Sn_2 kagome lattices. *Phys. Rev. Lett.* **121**, 096401 (2018).
- [22] M. Kang *et al.*, Dirac fermions and flat bands in the ideal kagome metal FeSn . *Nat. Mater.* **19**, 163-169 (2020).
- [23] Z. Liu *et al.*, Orbital-selective Dirac fermions and extremely flat bands in frustrated kagome-lattice metal CoSn . *Nat. Commun.* **11**, 4002 (2020).
- [24] M. Kang *et al.*, Topological flat bands in frustrated kagome lattice CoSn . *Nat. Commun.* **11**, 4004 (2020).
- [25] Y. Hu *et al.*, Topological surface states and flat bands in the kagome superconductor CsV_3Sb_5 . *Science Bulletin* **67**, 495-500 (2022).

[26] Y. Cao *et al.*, Correlated insulator behaviour at half-filling in magic-angle graphene superlattices. *Nature* **556**, 80-84 (2018).

[27] Y. Cao *et al.*, Unconventional superconductivity in magic-angle graphene superlattices. *Nature* **556**, 43-50 (2018).

[28] X. Lu *et al.*, Superconductors, orbital magnets and correlated states in magic-angle bilayer graphene. *Nature* **574**, 653-657 (2019).

[29] M. Yankowitz *et al.*, Tuning superconductivity in twisted bilayer graphene. *Science* **363**, 1059-1064 (2019).

[30] Y. Cao *et al.*, Tunable correlated states and spin-polarized phases in twisted bilayer-bilayer graphene. *Nature* **583**, 215-220 (2020).

[31] A. H. Castro Neto *et al.*, The electronic properties of graphene. *Rev. Mod. Phys.* **81**, 109-162 (2009).

[32] G. J. Miller, Solid state chemistry of Nb_3Cl_8 : Nb_3TeCl_7 , mixed crystal formation, and intercalation. *J. Alloys Compd.* **217**, 5-12 (1995).

[33] Y. Haraguchi *et al.*, Magnetic-nonmagnetic phase transition with interlayer charge disproportionation of Nb_3 trimers in the cluster compound Nb_3Cl_8 . *Inorg. Chem.* **56**, 3483-3488 (2017).

[34] S. N. Magonov *et al.*, Scanning tunnelling and atomic force microscopy study of layered transition metal halides Nb_3X_8 ($\text{X} = \text{Cl}, \text{Br}, \text{I}$). *J. Am. Chem. Soc.* **115**, 2495 (1993).

[35] J. R. Kennedy, P. Adler, R. Dronskowski, & A. Simon, Experimental and Theoretical Electronic Structure Investigations on α - Nb_3Cl_8 and the Intercalated Phase β' - NaNb_3Cl_8 . *Inorg. Chem.* **35**, 2276-2282 (1996).

[36] J. Yoon *et al.*, Anomalous thickness-dependent electrical conductivity in van der Waals layered transition metal halide, Nb_3Cl_8 . *J. Phys.: Condens. Matter* **32**, 304004 (2020).

[37] Sasioglu, E., Friedrich, C. & Blugel, S. Effective Coulomb interaction in transition metals from constrained random-phase approximation. *Phys. Rev. B* **83**, 121101(R) (2011).

[38] H. Wu *et al.*, The field-free Josephson diode in a van der Waals heterostructure. *Nature* **604**, 653-656 (2022).

[39] Y. Zhang, Y. H. Gu, J. P. Hu, & K. Jiang, General theory of Josephson diodes. *arXiv:2112.08901* (2021).

[40] G. Kresse, & J. Furthmuller, Efficient iterative schemes for ab initio total- energy calculations using a plane-wave basis set. *Phys. Rev. B* **54**, 11169 (1996).

[41] G. Kresse, & D. Joubert, From ultrasoft pseudopotentials to the projector augmented-wave method. *Phys. Rev. B* **59**, 1758 (1999).

[42] P. E. Blochl, Projector augmented-wave method. *Phys. Rev. B* **50**, 17953 (1994).

[43] J. Heyd, & G. E. Scuseria, Hybrid functionals based on a screened Coulomb potential. *J. Chem. Phys.* **118**, 8207 (2003).

[44] J. Heyd and G. E. Scuseria, Efficient hybrid density functional calculations in solids: Assessment of the Heyd-Scuseria-Ernzerhof screened Coulomb hybrid functional. *J. Chem. Phys.* **121**, 1187 (2004).

[45] G. Pizzi *et al.*, Wannier90 as a community code: new features and applications. *J. Phys. Condens. Matter* **32**, 165902 (2020).

[46] A. Georges, G. Kotliar, W. Krauth, & M. J. Rozenberg, Dynamical mean-field theory of strongly correlated fermion systems and the limit of infinite dimensions. *Rev. Mod. Phys.* **68**, 13 (1996).

[47] L. Huang *et al.*, iQIST: An open source continuous-time quantum Monte Carlo impurity solver toolkit. *Comput. Phys. Commun.* **195**, 140 (2015).

[48] E. Gull *et al.*, Continuous-time Monte Carlo methods for quantum impurity models. *Rev. Mod. Phys.* **83**, 349 (2011).

[49] M. Jarrell, & J. Gubernatis, Bayesian Inference and the Analytic Continuation of Imaginary-Time Quantum Monte Carlo Data. *Phys. Rep.* **269**, 133-195 (1996).

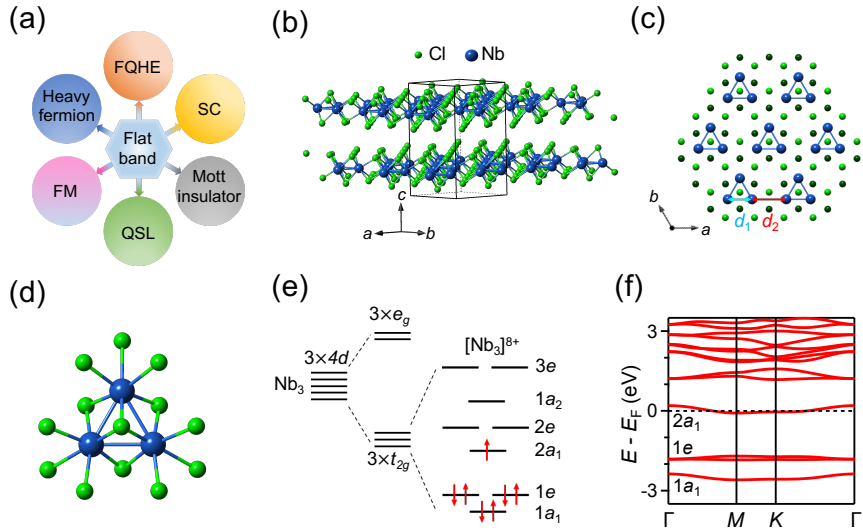


Fig. 1. Half-filled flat band in the vdW compound Nb₃Cl₈. (a) Emergent quantum phenomena in flat-band systems. FQHE, fractional quantum Hall effect; SC, superconductivity; QSL, quantum spin liquid; FM, ferromagnetism. (b) Crystal structure of the vdW compound Nb₃Cl₈. (c) Top view of the Nb₃Cl₈ monolayer showing Nb₃ trimers. Blue lines indicate the Nb–Nb metal bonds within each Nb₃ trimer. Dark- and light-green spheres represent the Cl atoms below and above the Nb atomic layer, respectively. (d) Top view of a Nb₃Cl₁₃ cluster composed of three edge-sharing NbCl₆ octahedra. (e) Schematic plot of the molecular orbitals, which are occupied by seven Nb 4d valence electrons, in an isolated Nb₃Cl₁₃ cluster. (f) Calculated electronic structure based on the HSE06 functional for monolayer Nb₃Cl₈.

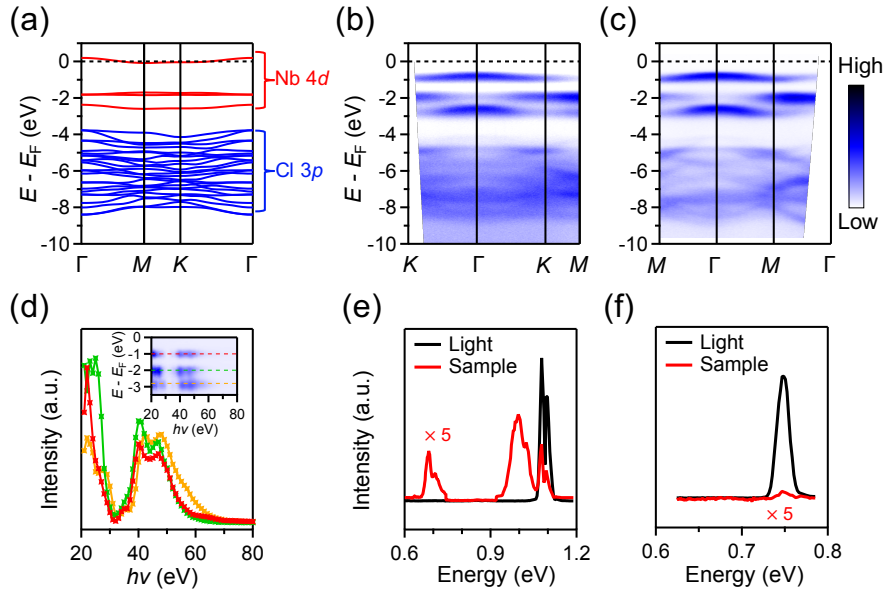


Fig. 2. Band gap at E_F revealed by ARPES and PL spectra. (a) Calculated valance bands based on the HSE06 functional for monolayer Nb_3Cl_8 . Red and blue curves represent the bands mainly from the Nd 4d and Cl 3p orbitals, respectively. (b),(c) Intensity plots of the ARPES data along Γ -K and Γ -M, respectively. (d) $h\nu$ dependence of the spectral intensities at three constant energies indicated by the dashed lines in the inset. Inset: Intensity plot of the ARPES data at the M point with varying $h\nu$. The spectral intensities are normalized by the photon flux. (e) PL spectrum of the sample (red curve) excited by 1.1-eV photons. Black curve is the spectrum of the pulsed laser for reference. The splitting of the peaks is due to the slit between pixels on the detector. (f) Same as in (e), but excited by 0.75-eV photons. The PL spectral intensities from the sample are multiplied by 5.

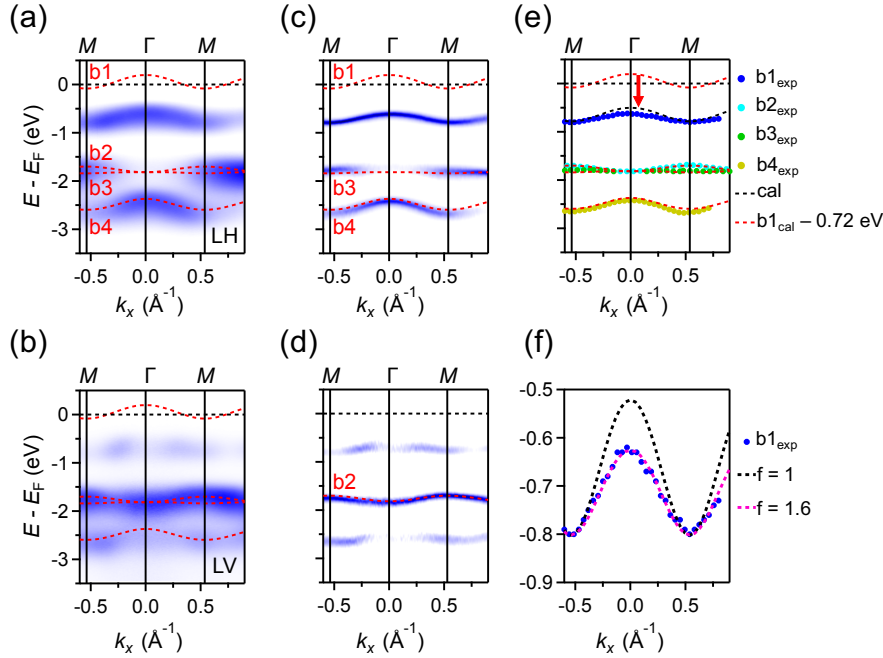


Fig. 3. Comparison between calculated and experimental band dispersions. (a),(b) Intensity plots of the ARPES data along Γ -M collected with linearly horizontal (LH) and linearly vertical (LV) polarizations of the incident light, respectively. Red dashed curves, which are denoted as b1, b2, b3, and b4, are the calculated bands based on the HSE06 functional. The ARPES spectra are shifted up by 0.2 eV to better match the calculations. (c),(d) Intensity plots of the curvature with respect to energy of the ARPES data in (a) and (b), respectively. (e) Comparison between the calculated and experimental bands. The experimental bands are extracted by tracking the peak positions of energy distribution curves of the ARPES data in (a) and (b). Black dashed curve is the calculated b1 band shift down by 0.72 eV as indicated by the red arrow. (f) Precise comparison between the experimental and calculated b1 bands. Black and pink dot curves represent the calculated b1 bands, which are not renormalized and renormalized by a factor of 1.6, respectively.

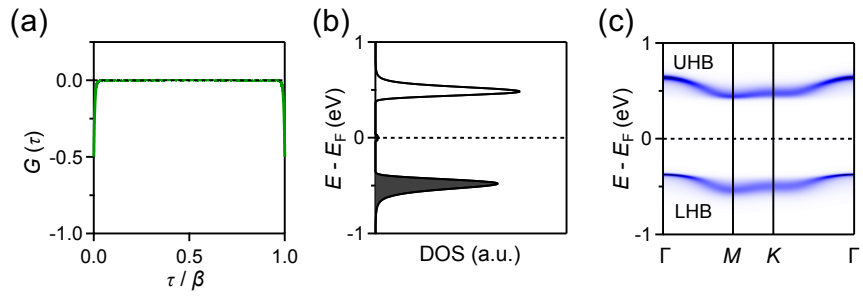


Fig. 4. Mott insulator state established by DMFT calculations. (a) Imaginary time Green's function with $U = 1$ eV. τ is the imaginary time. (b) DOS of the single-band Hubbard model with $U = 1$ eV. (c) Spectral function of the upper Hubbard band (UHB) and lower Hubbard band (LHB) along high-symmetry path.